The International Journal of Advanced Manufacturing Technology (2019) 102:2367–2374
https://doi.org/10.1007/s00170-019-03292-2

ORIGINAL ARTICLE

A mathematical model of the deposition rate and layer height during electrochemical additive manufacturing

Abishek B. Kamaraj[1] · Murali Sundaram[1]

Received: 18 October 2018 / Accepted: 2 January 2019 / Published online: 1 February 2019

Abstract
Electrochemical additive manufacturing (ECAM) is a novel non-thermal metal additive manufacturing technology. The layer height is an important parameter in additive manufacturing processes which determines the resolution and quality of the parts manufactured. The modeling of the rate of deposition enables the prediction of the layer size and time of deposition for a particular feature. The developed model takes the electrical process parameters and the horizontal scan speed as inputs and gives the rate of deposition and deposited layer height as the output. The current density was calculated based on an existing model considering ion transport and electrode kinetics. The predicted deposition rates were validated with experimental findings. It was found that the pulsed voltage with a 75% duty cycle had the highest deposition rate. While the deposition rates varied between 1 and 3 μm/s, the scan speed was found to be between 0.1 to 2 mm/s for a diameter 250-μm tool. The scan speed had a lower limit for each interelectrode gap below which a possibility of short-circuiting exists. The influence of the pulse duty cycle on the layer height reduces at larger interelectrode gaps.

Keywords Additive manufacturing · Electrochemical deposition · Layer height · Model

1 Introduction

The recent advancement of technology has increased the need for manufacturing processes capable of making smaller, highly customized parts. Additive manufacturing (AM) is increasingly being used to manufacture functional parts because of its ability to create highly complex, customized parts starting from a computer-aided design (CAD) [1]. AM processes have found wide acceptance in varied fields such as biomedical, aerospace, and electronics industries, due to their need for highly customized, unique parts [2–4]. A wide variety of materials can be manufactured using AM processes such as metals, polymers, and piezoceramic materials [5]. Some AM processes, such as selective laser melting (SLM), direct metal laser sintering (DMLS), and electron beam melting (EBM) can be used for manufacturing metal parts. However, the parts produced using these thermal-based AM processes have high residual stresses due to the melting and re-solidification of the part during manufacturing leading to thermal deformation and shrinkage [6, 7]. Many of these processes are also limited in their capability to produce micron scale features as they are limited by the powder size [1, 4]. Extensive heat treatment and post-processing are also required after these thermal processes to relieve these high thermal stresses [8].

Electrochemical additive manufacturing (ECAM) is a novel process that combines the principles of AM and localized electrochemical deposition (LECD) to produce metal parts at room temperature without thermal stress [9]. As the nature of deposition in ECAM is atom by atom as opposed to other traditional metal additive manufacturing processes, parts can be built with no need for support structures and by changing build orientation [10]. The process flow showing the manufacturing of a part without the need of support structure starting from the CAD model to the final manufactured part is given in Fig. 1. The parts produced during ECAM do not have any thermal-induced residual stresses as the process is non-thermal in nature. ECAM is also used in a micro-repair application with the use of electrolytes confined in liquid marbles [11].

Past studies have attempted to model LECD by simulating the current density and electric field through the electrolyte [12]. Three-dimensional structures made by LECD with deposition rates up to 6 μm/s have been reported [13]. Parts manufactured at a consistent deposition rate during LECD are expected to have better structure, surface finish, and more

✉ Murali Sundaram
murali.sundaram@uc.edu

[1] Department of Mechanical and Materials Engineering, University of Cincinnati, Cincinnati, OH 45220, USA

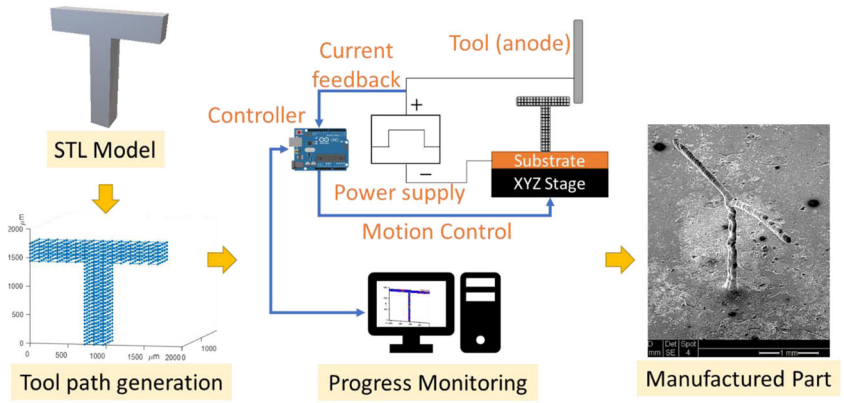

Fig. 1 Schematic of the process flow for ECAM starting from the part model file to the manufactured part

compact centers. A study of the withdrawing speed of the tool from nickel deposits during LECD found that the growth rate of the nickel deposits slows at a quadratic rate over time, and tool withdrawal from the deposition needs to change accordingly [14]. The influence of the voltage and interelectrode gap (IEG) on the deposition rates was experimentally studied in [15] with higher voltage and smaller IEG leading to higher deposition rates. Another study attempted to optimize tool withdrawal speed, where it was found that the optimal tool withdrawal speed should be the same as growth speed of the deposit, which lead to improved geometry confinement [16]. A 6.67% increase in deposition rates was seen using the rotating electrode as well as increased dimensional control [17].

Pulsed power during LECD has been reported to produce parts with higher strength when compared to parts made using DC power [18]. The reason for this was attributed to a unique microstructure with grains that contain a high density of layered nanoscale twins divided by coherent twin boundaries. The same study also found that while the peak current density during the pulsed LECD was higher, the average current density was higher in DC powered LECD [18]. The reason for higher peak current during pulsed LECD is due to the replenishment of the ions during the pulse off time [19].

Several numerical evaluations and simulation studies have used current values from the electric field to evaluate the relationship between the process variables on the deposition during LECD [1, 12, 20–25]. The current density and rate of deposition predicted by these studies often do not compare well with actual experimental values, possibly due to the lack of consideration of the ion migration, bubble-electrolyte two-phase interactions, and diffusion effects. An earlier study simulated the movement of the actual ions during electrochemical processes, however, did not analyze these behaviors throughout the entire ECAM process and did not account for the dynamic nature of the tool movement during ECAM [21]. A recent modeling study used a simplified analytical solution to the problem of the microcolumn deposition [24]. This study predicted the conditions under which either tubular or cylindrical structures are formed during LECD. Experimental studies of LECD that undergo separate horizontal and vertical motion of the anode have mostly used current based feedback to estimate and control the layer height [9, 10, 26].

The experimental deposition rates observed during LECD have generally been calculated only for the direction normal to the substrate with the anode motion considered only in the vertical Z direction. However, in ECAM, the anode (tool) moves in all the three (XYZ) axes resulting in 3D shapes being deposited. Thus, there is a need to predict the layer height of the deposit in terms of the scan speed in the horizontal (X- or Y-axis) direction. Modeling of the layer height and the rate of deposition during ECAM considering ion transport and under pulse power conditions has not been reported in prior literature. Thus, in this paper, the deposition rate and layer height have been modeled using current density predicted based on ion transport calculations for the ECAM process. The effect of pulse characteristics, electrolyte concentration, and the interelectrode gap has been modeled. The variations in the deposit height due to the velocity change in the X-Y horizontal direction of the anode has been analyzed. This application of the model cuts the time-consuming trial and error approach generally associated with electrochemical deposition. The model can also be used to predict the required input process parameters needed to achieve a user-defined layer height. Layer height is one of the parameters in additive manufacturing which determines the resolution of the parts produced, with smaller layer height leading to more fine features being manufactured.

2 Mathematical model

2.1 Rate of deposition model

From Faraday's law, the volume of nickel (V_{Ni}) deposited can be derived as

$$V_{Ni} = \frac{\epsilon M_{Ni} I t}{\rho_{Ni} n_{Ni} F} \tag{1}$$

where M_{Ni} is the molar mass of nickel (g/mol), I is the average deposition current (A), t is the deposition time (s), ρ_{Ni} is the

density of nickel (kg/m^3), n_{Ni} is the valency of nickel, ϵ is the current efficiency, and F is the Faraday's constant. Assuming a constant deposition cross-sectional area equal to the bottom surface area of the tool and differentiating the equation with respect to time, we arrive at the rate of deposit height increase as

$$\frac{dh}{dt} = \frac{\epsilon M_{Ni} i(t)}{\rho_{Ni} n_{Ni} F} \tag{2}$$

where $i(t)$ is the instantaneous current density. The current density was calculated based on the flux density of the species at $h = 0$ as given in the Eq. (3).

$$i(t) = n_{Ni} F D \frac{\partial C}{\partial h} \tag{3}$$

The concentration C, of the nickel cations, was estimated based on the model developed in [19]. It is briefly described below.

The one-dimensional mass transfer governing equation for nickel diffusion is given by Fick's law of diffusion as shown in Eq. (4).

$$\frac{\partial C}{\partial t} = D \frac{\partial^2 C}{\partial h^2} \tag{4}$$

The boundary and initial conditions, as illustrated in Fig. 2, are given in the equations below:

$$C(h, 0) = C_\infty \tag{5}$$

$$C(h_G, t) = C_\infty \tag{6}$$

$$\left.\frac{\partial C}{\partial h}\right|_{h=0} = \frac{i_0}{nFD}\left[\frac{C_{(0,t)}}{C_\infty} 10^{\left(\frac{\alpha_c F}{2.3RT}\eta\right)} - 10^{-\left(\frac{\alpha_a F}{2.3RT}\eta\right)}\right] \tag{7}$$

where C is the instantaneous concentration of nickel cation, t is the time, h is the vertical distance from the cathode, D is the diffusivity of the cation, C_∞ is the bulk electrolyte concentration, i_0 is the exchange current density, α_c is the cathodic charge transfer coefficient, R is the universal gas constant, T is the temperature, $\alpha_a$is the anodic charge transfer coefficient, h_G is the interelectrode gap, and η is the applied overpotential. η is a function of time with varying values based on the frequency and duty cycle of the applied pulse voltage. A detailed discussion on the effect of a change in pulse conditions on the current density and the numerical solution to Eq. (4) is available elsewhere [19]. Substituting the average steady-state current density calculated by solving for the concentration variation in the interelectrode gap (IEG) from Eq. (3) to Eq. (2) leads to the rate of deposition as

$$\frac{dh}{dt} = \frac{\epsilon M_{Ni} D \frac{\partial C}{\partial h}}{\rho_{Ni}} \tag{8}$$

2.2 Layer height estimation model

Given the assumption that only the surface beneath the tool (anode) undergoes deposition, the layer height can be determined as the product of the deposition rate and the time spent by any point on the cathode surface beneath the tool electrode as given below.

$$h_L = \frac{dh}{dt} \times t_{tool} \tag{9}$$

where t_{tool} is the time taken by the tool to pass any point on the cathode below. t_{tool} is directly proportional to the width of the tool (L_w) while being inversely proportional to the scan speed (v_s) as shown below

$$t_{tool} = \frac{L_w}{v_s} \tag{10}$$

Substituting Eqs. (8) and (10) in (9) results in the final model for the layer height as

$$h_L = \frac{\epsilon M_{Ni} D \frac{\partial C}{\partial h}}{\rho_{Ni}} \times \frac{L_w}{v_s} \tag{11}$$

This model enables the control of the velocity at which the anode moves in order to achieve the desired deposit height during the horizontal movement in ECAM. Thus, the tool velocity will be faster at places where the lesser deposition is required and slower when more material is needed. This

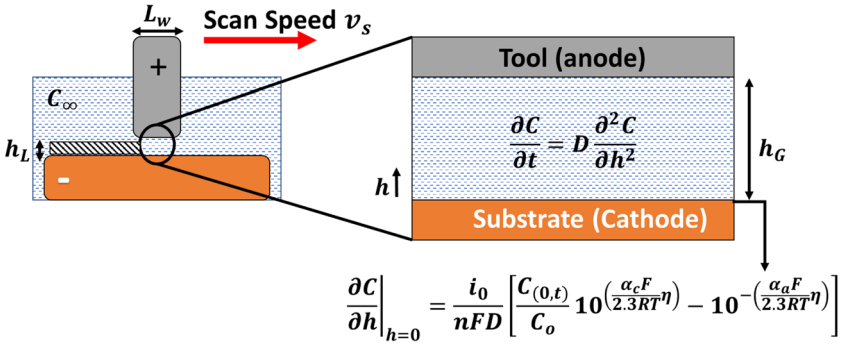

Fig. 2 Schematic of the ECAM model showing boundary conditions, layer height, and scan speed direction

allows for flexibility in the process of material deposition, as the required amount of material deposited is controlled.

Assumptions considered while arriving at the layer height estimation model are as follows:

- Only surfaces directly below the anode undergo deposition, i.e., no deposition occurs in the cathode profile further away from the anode.
- Heat generation effects are neglected as the deposition is considered to be in the micron scale and the tool is in constant motion.
- Current efficiency (ϵ), overpotential (η), and electrolytic conductivity (κ_e) are considered to be constants during the pulse-on time.
- Cathode moving with constant velocity along the horizontal axis.
- The length of anode L_w is small relative to the surface variations.

The process parameters and constants used for the deposition rate and layer height model are given in Table 1.

3 Theoretical model predictions and discussion

3.1 Rate of deposition model predictions

3.1.1 Effect of duty cycle and IEG

The model predictions of the rate of deposition under varying duty cycles and IEG are shown in Fig. 3. The rate of deposition increases with duty cycle up to 75%. The rate decreases from 75% to no pulse (100%) condition. This indicates that pulse power is preferable for the deposition if we require a higher rate of deposition. The replenishment of the cation concentration during the off time is the reason for the higher rate of deposition as there are more ions to be deposited. At lower duty cycles, the average deposition rate is lower due to the smaller on times even though the peak current density during the pulse-on time is higher at lower duty cycles.

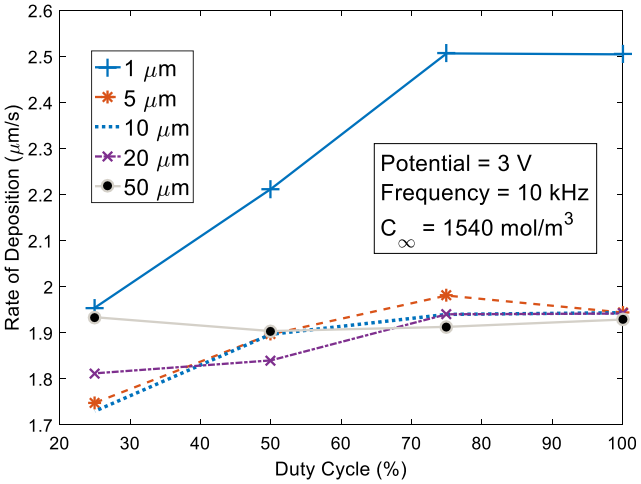

Fig. 3 The model-predicted rate of deposition under varying duty cycles and interelectrode gaps

IEG of 1 μm results in the highest rate of deposition as seen in Fig. 3. Lower IEG leads to an increase in the current density as there is a lower electrolyte resistance. This is due to the fact that the resistance of the electrolyte is directly proportional to the IEG. At IEG values greater than 20 μm, the influence of duty cycle diminishes. In Fig. 3, this is reflected in the 50-μm IEG line showing no change in the rate of deposition under changing duty cycles. This is because at very high IEGs, the depletion region is not fully formed due to the large availability of the ions for deposition leading to lowering the influences of pulse power. Also, the effect of the large resistance nullifies the effect of pulsed power.

Table 1 Process parameters used in the deposition rate and layer height determination model

Parameter	Value
D (m^2 s^{-1})	7×10^{-10} [27]
C_∞ (mol m^{-3})	1540
n_{Ni}	2
i_0 (A cm^{-2})	6.7×10^{-3} [28]
$\frac{\alpha_c F}{2.3RT}$ (V^{-1})	4.17 [28]
$\frac{\alpha_a F}{2.3RT}$ (V^{-1})	25 [29]
η (V)	3
Frequency (kHz)	5, 10, and 100 kHz
Duty cycle	25, 50, 75, and 100%
h_G (μm)	1–50
ϵ	0.35
v_s (mm/s)	0.1–2
L_w (μm)	250

3.1.2 Effect of frequency

The rate of deposition predicted under varying pulse frequencies and the duty cycle is given in Fig. 4. The frequency changes showed a very little effect on the rate of deposition under varying duty cycles at the 1-μm IEG (Fig. 4a). It was found that the 10-kHz frequency showed a higher rate of deposition when compared to both 5 and 100 kHz at both the 1- and 5-μm IEGs. This shows that at high frequencies, the ions do not have enough time to replenish during the pulse off time, while at lower frequencies, the on time is too long leading to lower overall current densities and rate of deposition. At larger IEG above 20 μm, the influence of duty cycle diminished at the 10- and 100-kHz frequencies. At the 5-kHz frequency, the rate of deposition still showed an increasing trend with duty cycle. This is because unlike the high-frequency deposition,

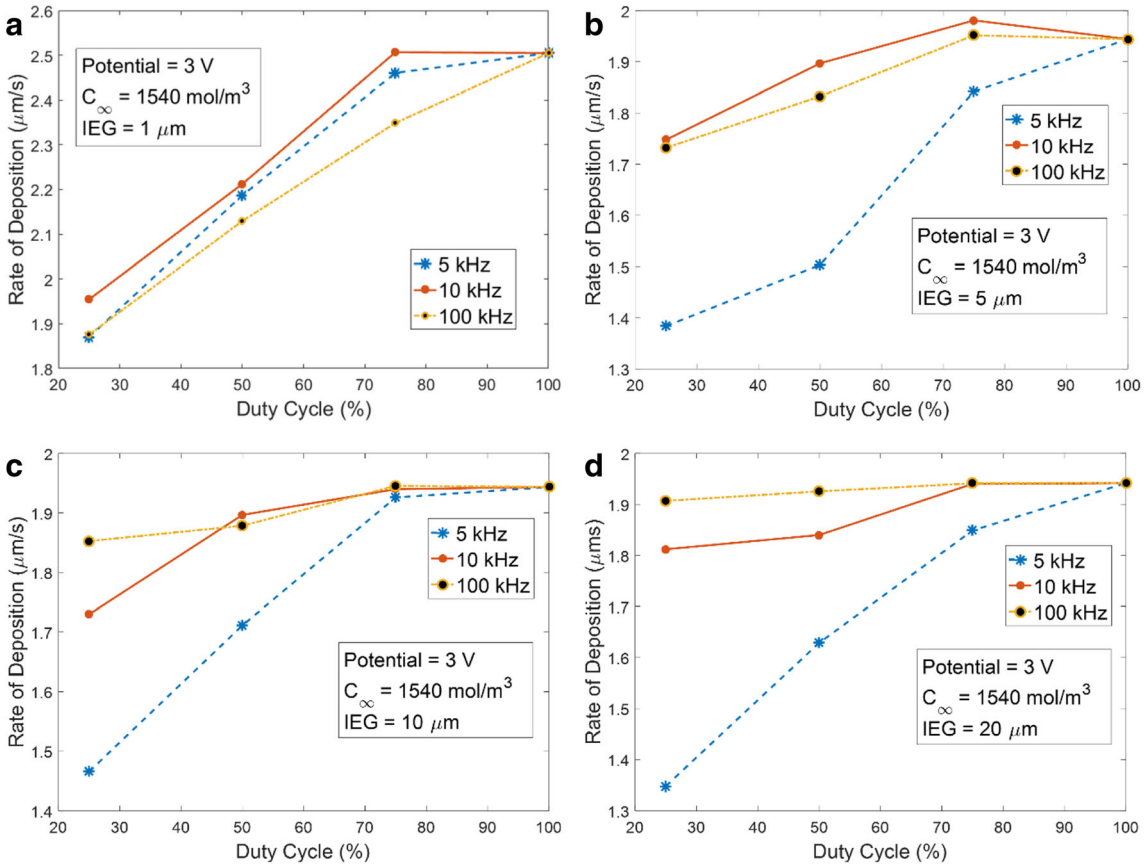

Fig. 4 The model-predicted rate of deposition under different frequencies, duty cycle, and IEG of the applied voltage **a** 1 μm IEG, **b** 5 μm IEG, **c** 10 μm IEG, and **d** 20 μm IEG

the longer on time and off time at lower frequencies allow for the current density to vary with the pulse conditions.

3.2 Layer height model predictions

The scan speed is inversely correlated to the layer height as per the model (Fig. 5). The faster the scan speed is, the lower the layer height of the deposit. The scan speed has a lower limit based on the interelectrode gap. This is around 0.1 mm/s for a 5-μm gap at a 3-V pulse power and a 250-μm tool width. This lower limit is near 0.75 mm/s for the 1-μm IEG, 0.05 mm/s for the 10-μm IEG, and 0.025 mm/s for the 10-μm IEG under similar conditions. Any speed slower than this value will result in the deposition reaching the anode during the deposition process leading to short circuits which are undesirable. The influence of the varying duty cycles on the layer height reduces with an increase in the scan speed. At lower scan speeds, the layer height predictions match the trends for the rate of deposition. The highest layer height is found to be at a duty cycle of 75% corresponding to the highest rate of deposition. The scan speed is several orders of magnitude higher than the vertical rate of deposition for a 250-μm tool. Larger tools, even at high scanning speed, will hover over any individual point in the deposition region for sufficient time to complete the deposition. However, for smaller tools, to ensure their presence over the same point in the deposition region for the same amount of time, the scanning speed needs to be reduced.

4 Experimental validation

4.1 Experimental validation of the rate of deposition model

The rate of deposition was studied experimentally using the setup shown in Fig. 6 to validate the model results. A platinum/microelectrode, with diameter Ø 250 μm, insulated on the sides was used as the anode. The tool was insulated using a room temperature cured enamel paint which resulted in an insulation thickness of 250–500 μm. The tooltip was polished after every experiment to maintain the flatness of the disk shape and remove any debris from the deposition. A 2-cm × 2-cm brass plate, with a 500-μm thickness was used as the cathode substrate. Pulse power was provided using an arbitrary function generator. An Arduino controlled three-axis micro-stage was used for the motion control. The Arduino was also used as a current monitoring and feedback controller using an in-house developed algorithm and code. The controller is capable of

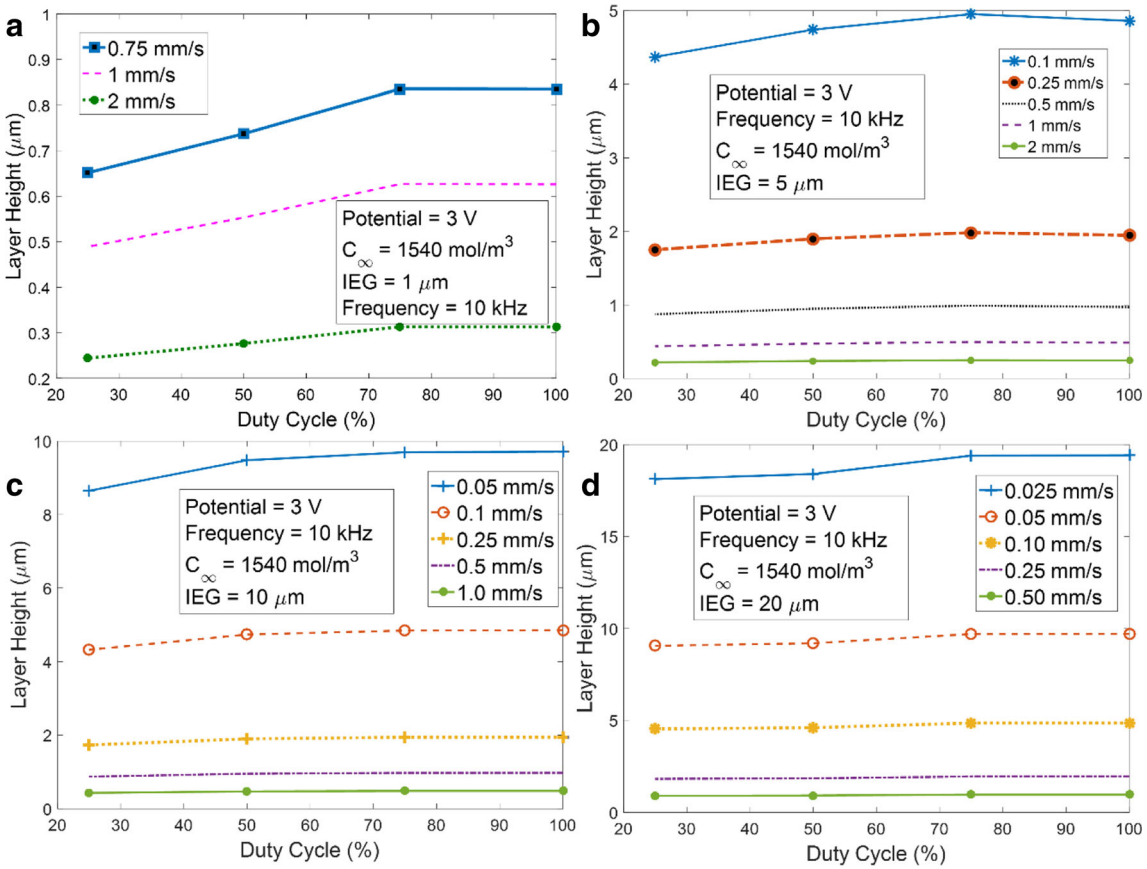

Fig. 5 Layer height estimated by the model under varying scan speeds and duty cycle **a** 1 μm IEG, **b** 5 μm IEG, **c** 10 μm IEG, and **d** 20 μm IEG

detecting the short circuits which indicate that the deposit has reached the anode. Pulse power from an arbitrary function generator was used to generate the required high-frequency pulses. Duty cycle is defined as the percentage of time the pulse power is on (t_{on}) to the total time period of the pulse ($t_{on} + t_{off}$). DC power supply was used to power the process with 100% duty cycle. Watts's bath was used as the electrolyte which contains nickel sulfate (240 g), nickel chloride (45 g), and boric acid (30 g) per liter of distilled water. This formulation of the electrolyte was used as this was known to have lower throwing power which is good for localizing the deposit [30]. Boric acid acts as a pH buffer for the electrolyte. While nickel sulfate provides the majority of the cations needed for the deposition, nickel chloride aides in the deposition of fine-grained nickel with improved microstructure [31]. The tool (anode) was kept stationary, and deposition occurred until the deposit touched the tip of the tool. This process was repeated for different IEGs as the current in the system was monitored. Fifteen replications of the trials were performed at each IEG to account for the experimental deviations. The micro-stages have a step size resolution of 1.5 μm. This was used during the deposition to achieve the required IEG. After the deposition, we used scanning electron microscope images as well as a surface profilometer to analyze the height of the deposit.

Fig. 6 Experimental setup

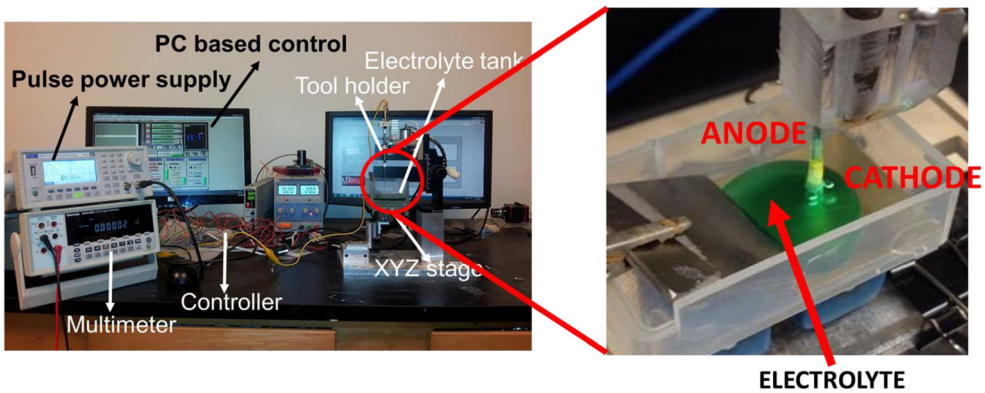

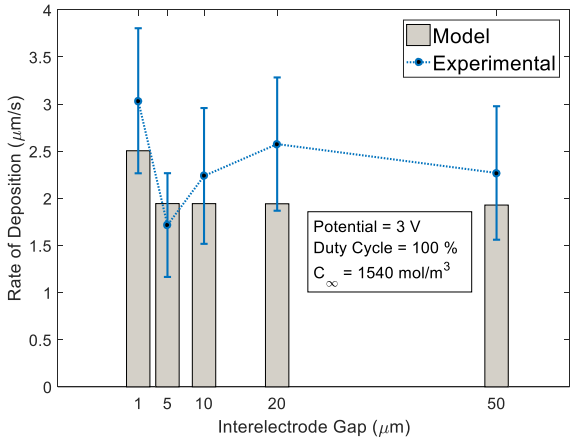

Fig. 7 Comparison of model predictions of the rate of deposition with experimental findings

To validate the rate of deposition, the amount of time taken to deposit was recorded. The rate of deposition was calculated as the deposit height divided by the time to deposit the part. These values were compared to the rate of deposition predicted by the model (Fig. 7). From the validation experiments, it is clear that that the model predicts the rate of deposition over the wide range of IEG well with the predicted values being within the range of experimental deviations. The model predicts a higher rate of deposition at very small IEG (near 1 μm) with the rate becoming a constant at higher IEG. This similar trend is seen with the experimental results at higher IEG of 10, 20, and 50 μm.

4.2 Experimental validation of the layer height model

To validate the layer height model, horizontal lines were deposited on top of the substrate under constant scan speeds. The IEG was set at a constant 10 μm. The tool size used for this deposition was a side insulated tool with a 50-μm diameter tool electrode. The scan speed varied between 5 and 50 μm/s. The layer height of the deposited line was measured after each of these experiments using a surface profilometer. The layer height was measured at three different locations and the average value is reported in Fig. 8. The layer height showed an exponential decrease with increasing scan speeds. The experimental trend of smaller layer height with increasing scan speeds matches with the model predictions as shown in Fig. 8. The model overestimates the deposit layer height in all the instances. This might be because the model does not consider the impedance effects caused by the bubbles generated as well as experimental deviations caused by the resolution of the stage. The model prediction for the scan speeds of 5 and 7.5 μm/s is more than the IEG indicating that the model is predicting short-circuiting due to the contact of the deposit with the tool. Still, the model captures the exponential reducing trend as seen in the experiments.

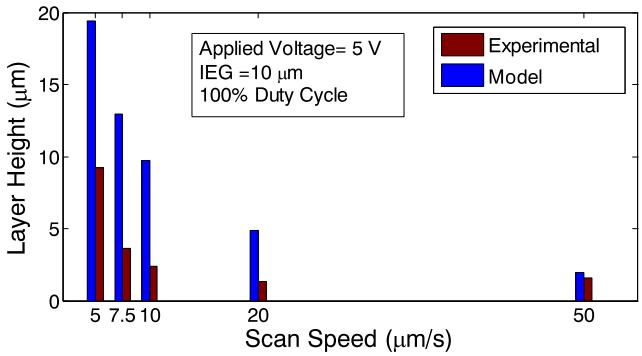

Fig. 8 Comparison of the layer height estimated by the model with the experimental findings for varying scan speeds

5 Conclusions

The influence of the pulsed power settings and the scan speed on the rate of deposition and deposit layer height during ECAM were modeled in this study. It was found that pulsed power at 75% duty cycle had the highest deposition rate when compared to DC (100%) as well as lower duty cycles. Even though the lower duty cycles showed higher peak current densities, the average rate of deposition was highest at 75% duty cycle. The benefits of the pulse power were reduced at higher interelectrode gaps due to the availability of ions at large gaps. The frequency of the pulse power had a lower effect on the rate of deposition when compared to the duty cycle and IEG in the ECAM process. The horizontal scan speeds associated with ECAM were found to be several orders of magnitude higher than the deposition rate for our process conditions. The layer height predicted was influenced significantly by the scan speed. It was found that there is a minimum scan speed associated with any particular value of IEG. The developed model for the rate of deposition and layer height estimation was validated with experiments.

Funding information This material is based upon work supported by the National Science Foundation under Grant Nos. CMMI-1400800 and CMMI-1454181.

References

1. Vaezi M, Seitz H, Yang S (2012) A review on 3D micro-additive manufacturing technologies. Int J Adv Manuf Technol 67:1721–1754
2. Stansbury J, Idacavage M (2016) 3D printing with polymers: challenges among expanding options and opportunities. Dent Mater 32:54–64
3. Shapiro A, Borgonia J, Chen Q, Dillon R, McEnerney B, Polit-Casillas R, Soloway L (2016) Additive manufacturing for aerospace flight applications. J Spacecr Rocket 53:952–959
4. MacDonald E, Wicker R (2016) Multiprocess 3D printing for increasing component functionality. Science 353:aaf2093
5. Chabok H, Zhou C, Chen Y, Eskandarinazhad A, Zhou Q, Shung K (2012) Ultrasound Transducer Array Fabrication Based on Additive Manufacturing of Piezocomposites. ASME. International Symposium on Flexible Automation, ASME/ISCIE 2012

International Symposium on Flexible Automation pp. 433–444. https://doi.org/10.1115/ISFA2012-7119
6. Kruth JP, Froyen L, Van Vaerenbergh J, Mercelis P, Rombouts M, Lauwers B (2004) Selective laser melting of iron-based powder. J Mater Process Technol 149:616–622
7. Roberts IA, Wang CJ, Esterlein R, Stanford M, Mynors DJ (2009) A three-dimensional finite element analysis of the temperature field during laser melting of metal powders in additive layer manufacturing. Int J Mach Tools Manuf 49:916–923
8. Cabrini M, Lorenzi S, Pastore T, Pellegrini S, Ambrosio P, Calignano F, Manfredi D, Pavese M, Fino P (2016) Effect of heat treatment on corrosion resistance of DMLS AlSi10Mg alloy. Electrochim Acta 206:346–355
9. Sundaram MM, Kamaraj AB, Kumar VS (2015) Mask-less electrochemical additive manufacturing: a feasibility study. J Manuf Sci Eng 137:021006–021015
10. Brant A, Sundaram M (2016) A novel electrochemical micro additive manufacturing method of overhanging metal parts without reliance on support structures. Proc Manuf 5:928–943
11. Shailendar S, Sundaram M (2016) A feasibility study of localized electrochemical deposition using liquid marbles. Mater Manuf Process 31:81–86
12. Brant AM, Sundaram MM, Kamaraj AB (2015) Finite element simulation of localized electrochemical deposition for maskless electrochemical additive manufacturing. J Manuf Sci Eng 137: 011018–011018
13. Madden JD, Hunter IW (1996) Three-dimensional microfabrication by localized electrochemical deposition. J Microelectromech Syst 5:24–32
14. Yeo S, Choo JH, Yip KS (2000) Localized electrochemical deposition: the growth behavior of nickel microcolumns. In Micromachining and Microfabrication Process Technology VI. International Society for Optics and Photonics. 4174:30–40.https://doi.org/10.1117/12.396421
15. Wang F, Sun J, Liu D, Wang Y, Zhu W (2017) Effect of voltage and gap on micro-nickel-column growth patterns in localized electrochemical deposition. J Electrochem Soc 164:D297–D301
16. Said RA (2004) Adaptive tip-withdrawal control for reliable microfabrication by localized electrodeposition. J Microelectromech Syst 13:822–832
17. Yeo SH, Choo JH (2001) Effects of rotor electrode in the fabrication of high aspect ratio microstructures by localized electrochemical deposition. J Micromech Microeng 11:435–442
18. Daryadel S, Behroozfar A, Morsali SR, Moreno S, Baniasadi M, Bykova J, Bernal RA, Minary-Jolandan M (2018) Localized pulsed electrodeposition process for three-dimensional printing of Nanotwinned metallic nanostructures. Nano Lett 18:208–214
19. Kamaraj AB, Sundaram M (2018) A study on the effect of inter-electrode gap and pulse voltage on current density in electrochemical additive manufacturing. J Appl Electrochem 48:463–469
20. Said RA (2003) Microfabrication by localized electrochemical deposition: experimental investigation and theoretical modelling. Nanotechnology 14:523–531
21. Kamaraj A, Lewis S, Sundaram M (2016) Numerical study of localized electrochemical deposition for micro electrochemical additive manufacturing. Procedia CIRP 42:788–792
22. Said RA (2003) Shape formation of microstructures fabricated by localized electrochemical deposition. J Electrochem Soc 150: C549–C557
23. Wang F, Wang F, He H (2016) Parametric electrochemical deposition of controllable morphology of copper micro-columns. J Electrochem Soc 163:E322–E327
24. Volgin VM, Kabanova TB, Davydov AD (2018) Modeling of local maskless electrochemical deposition of metal microcolumns. Chem Eng Sci 183:123–135
25. Volgin VM, Lyubimov VV, Gnidina IV, Davydov AD, Kabanova TB (2018) Simulation of localized electrodeposition of microwires and microtubes. Procedia CIRP 68:242–247
26. Wang F, Bian H, Wang F, Sun J, Zhu W (2017) Fabrication of micro copper walls by localized electrochemical deposition through the layer by layer movement of a micro anode. J Electrochem Soc 164: D758–D763
27. Cui CQ, Lee JY (1994) Effects of oxygen reduction on nickel deposition from unbuffered aqueous solutions: I. Deposition Process Deposit Struct J Electrochem Soc 141:2030–2035
28. Ibrahim MAM (2006) Black nickel electrodeposition from a modified Watts bath. J Appl Electrochem 36:295–301
29. Popov K, Keča D, Vidojković S, Lazarević B, Milojković V (1976) Mathematical model and digital simulation of pulsating overpotential copper electrodeposition. J Appl Electrochem 6:365–370
30. Abdel-Hamid Z (1998) Improving the throwing power of nickel electroplating baths. Mater Chem Phys 53:235–238
31. Wesley WA, Carey JW (1939) The electrodeposition of nickel from nickel chloride solutions. Trans Electrochem Soc 75:209–236